Closed-Loop Control of Particles Based on Dielectrophoretic Actuation

Alexis Lefevre*, Vladimir Gauthier*, Michaël Gauthier and Aude Bolopion

The dielectrophoresis phenomenon exerts a force on dielectric particles placed in an inhomogeneous electric field. Using this property, we are able to control the displacement of microparticles by controlling the electric field in the workspace. It is achieved with an independent control of the voltages applied on electrodes placed inside a micro-chip. However, this type of system is characterized by a high non-linearity regarding the position and the input voltages, making the control difficult. In our previous work, we proposed a new model based on Fourier series to compute the electric potential produced by electrodes. Here, we extend this model to compute the dielectrophoretic force applied to particles and, propose a closed-loop controller based on the inversion of this model to achieve trajectory control of micrometer-size particles. This inversion, based on the simulated annealing technique, is implemented and tested on simulations and experiments. The main issues for the implementation of closed-loop control on the experimental platform are discussed and overcome. Experiments are performed on microbeads of 10 micrometers in diameter and confirm that the inverse model computes the required voltages. The trajectory control of micro-particles using closed-loop control at a frequency of 160 Hz is successfully achieved with a precision below 2 μm.

Index Terms—**Non-contact micromanipulation, dielectrophoresis, position and speed control, closed-loop, simulated annealing**

I. INTRODUCTION

NON-contact actuation for the manipulation of micrometer-size particles has gained a large interest during these last years. To achieve untethered micromanipulation, several physical principles can be used, such as magnetic actuation [1], [2], optical tweezers [3], acoustic waves [4] or electric fields [5]. Electric fields can be used for many purposes. They can induce fluid flows by electro-osmosis or electro-thermal effects [6], they can also be used to characterize micrometer-size particles [7], to manipulate micrometer size particles by electrophoresis or dielectrophoresis [8], and can be applied on living or non-living dielectric-particles. The precise control of particles, using electric-based micromanipulation platforms,

is currently an active field of research. Closed-loop control of dielectrophoresis-based micromanipulation platform has been investigated.

In [9], Kharboutly *et al.* used a micro-chip with four electrodes creating a limited control area to perform motion control of particles. The voltage applied on each electrode is independently controlled to generate complex configurations of electric field. A database linking the voltages applied to the electrodes and the dielectrophoretic force in this area was pre-processed to reduce computing time. Thus, with a simplified model and a PID controller, they completed the motion control of particles of 80 micrometers in diameter at high velocity (1000 μm/s).

More recently, Hurak *et al.* have proposed several models for dielectrophoresis-based micromanipulation platforms, dedicated to the implementation of closed-loop control [10], [11]. One of this model is based on the concept of Green's function to pre-process data of the electric voltages and their derivatives. During the closed-loop control, those data are used to quickly calculate the DEP force. To generate the electric field, they use an array of 48 electrodes and control the phase shift between each electrode. With this method, they manage to control the motion of particles of 50 μm in diameter at a closed-loop frequency of 10 Hz and a precision of 8 μm. They have also demonstrated orientation and position control of objects around 100 μm with non-spherical shapes, using 4 electrodes and a model combining electrokinetic and hydrodynamic effects running at 50 Hz [12].

In the biomedical field, there is a growing need to individually control and characterize cells [13]. Most of the time this has to be done inside micro-fluidic channels where the cells are carried by a high speed flow. Most of devices listed before are designed for artificial objects around 100μm in diameter with low dynamics or for control in a limited area making it difficult to use for most applications. We proposed in a previous work to overcome those limitations by using a new model based on Fourier series to compute the electric potential generated by parallel electrodes [14]. It appears that our model is a good option with regard to memory storage, computation time and precision with numerous electrodes. The use of parallel electrodes also make it possible to have a large area of control. This article investigates the use of this model to achieve closed-loop control at high speed on cell-sized particles. To reach this goal, the model must be inverted to compute the required voltages in order to produce a given motion of the particle. This inversion is complex due to the non-linearity of the model, the high number of electrodes, and the requirements in terms of computation time. We propose to use an optimization technique to invert
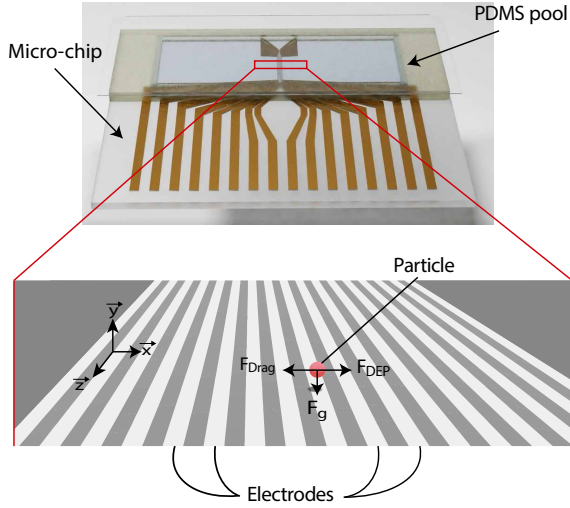
Fig. 1. General architecture of the studied system: the top part represents the micro-chip composed of parallel electrodes and the PDMS pool containing the solution with beads. The bottom part is a zoom on the control area where the electrodes are represented in white and the particle to control in red. The spherical particle in the center will undergo the drag force, the dielectrophoretic force and the gravity-buoyancy in the $(\vec{x}, \vec{y})$ plane.

this model. Due to the presence of local minima, we chose to use the simulated annealing technique. Closed-loop control is implemented based on a visual feedback and experiments are performed where the position of objects of $10\,\mu$m is controlled along a pre-defined trajectory.

The rest of the paper is organized as follows. Section II describes the dynamic model. The validation of the direct model through simulation and experiment is presented in section III. The inversion of the model is explained in section IV. The chosen parameters and results of the closed-loop control are discussed in section V. Finally, section VI concludes the paper.

II. DIRECT MODEL DEFINITION

This section recalls the basic principles of the model developed in [15]. The studied system is composed of a micro-chip with parallel electrodes used to produce dielectrophoretic actuation. This configuration is inspired from travelling wave control [16]. However, we propose here to independently control the voltage on each electrode. Parallel electrodes have proved to be of interest in the framework of micro-manipulation, as demonstrated in recent work [17]. In this configuration, electrodes can be considered as infinite compared to the size of the particles (Fig. 1). The dielectrophoretic force is perpendicular to the long axis of the electrodes, inducing the lateral displacement of the particle ($\vec{x}$ axis) as well as a displacement along its vertical direction ($\vec{y}$ axis). The motion of the particle on the longitudinal $\vec{z}$ axis is controlled only by the fluid. It is thus possible to decouple the motion along the $\vec{z}$ axis, induced by the fluid, and along the $\vec{x}$ and $\vec{y}$ axes, induced by the dielectrophoretic force. In the following sections, we only consider the motion of the particle due to the dielectrophoretic force.

In the general case, the forces applied to a particle are the fluid drag force, the gravity-buoyancy, the dielectrophoretic force and the Brownian motion. Moreover, the medium can be subjected to AC electro-osmosis and electrothermal flow. It can be shown that AC electro-osmosis, Brownian motion and electrothermal flow are at least two orders of magnitude less than the dielectrophoretic force, and one order of magnitude less than the joint effect of gravity and buoyancy [14]. Thus, these three effects are neglected in this work.

For a spherical particle around $10\,\mu$m in diameter subject to gravity-buoyancy $\vec{F}_g$, dielectrophoresis $\vec{F}_{\text{DEP}}$ and fluid drag $\vec{F}_{\text{drag}}$, Kharboutly *et al.* demonstrated that the inertial term can be neglected in Newton's second law [18]. Thus, we can consider that the particle undergoes three forces (see Fig. 1) and its motion can be deduced from:

$$\begin{bmatrix} 0 \\ 0 \end{bmatrix} = \mathbf{F}_g + \mathbf{F}_{\text{drag}} + \mathbf{F}_{\text{DEP}} \tag{1}$$

The gravity-buoyancy force is given by:

$$\mathbf{F}_g = \begin{bmatrix} 0 \\ \frac{4}{3}\pi a^3 (\rho_{\text{m}} - \rho_{\text{p}})g \end{bmatrix} \tag{2}$$

where a is the radius of the particle, ρ_m (resp ρ_p) is the fluid density (resp. particle density) and g is the gravitational acceleration. The next sections present the expressions of the drag and dielectrophoretic forces.

A. Model of the drag force

The Stockes' law gives the classical model of the drag force applied to a spherical particle. An extended version of this law, taking into account the boundary condition, has been proposed in [19], [20]:

$$\mathbf{F}_{\text{drag}} = \mathbf{D}.\dot{\mathbf{X}} \tag{3}$$

with

$$\mathbf{D} = -6\pi\mu a \begin{bmatrix} \lambda_x & 0 \\ 0 & \lambda_{\text{y}} \end{bmatrix}, \dot{\mathbf{X}} = \begin{bmatrix} \dot{x} \\ \dot{y} \end{bmatrix} \tag{4}$$

where $\mathbf{D}$ is an invertible matrix. μ is the dynamic viscosity, $\dot{x}$ (resp $\dot{y}$) is the particle velocity on the $\vec{x}$ (resp $\vec{y}$) direction. λ_{x} and λ_{y} are correction factors enabling to model the impact of the substrate close to the particle. These correction factors are defined in [19, Eq. (1)] and [20, Eq. (3.2)]:

$$\lambda_x = \left[1 - \frac{9}{16}\frac{a}{y} + \frac{1}{8}\left(\frac{a}{y}\right)^3 \right]^{-1}, \tag{5}$$

$$\lambda_y = \frac{8}{15}\sinh\alpha \left[\frac{2\sinh 3\alpha + 3\sinh 2\alpha}{4\sinh^2 1.5\alpha - 9\sinh^2\alpha} - 1 \right], \tag{6}$$

where

$$\alpha = \cosh^{-1}(1 + (y-a)/a),$$

and y is the altitude of the center of gravity of the particle above the substrate. As the drag coefficients are different along $\vec{x}$ and $\vec{y}$, this general model is called "anisotropic drag force" in the following of this paper. The isotropic classical Stockes' law corresponds to the case of $\lambda_x = \lambda_y = 1$.
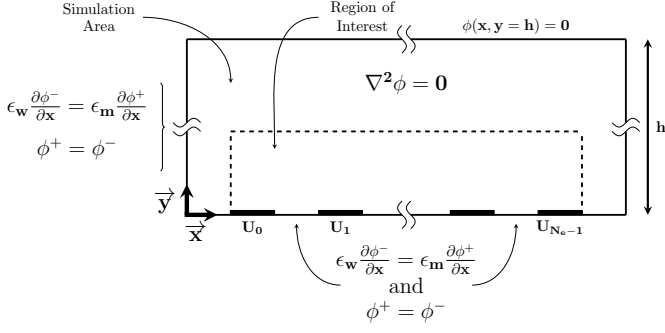
Fig. 2. Schematic representation of the boundary conditions determining the electric potential above an array of electrodes. ϕ^+ and ϕ^- are the electric potentials on each side of the boundary. ϵ_m is the permittivity of the fluid in the channel and ϵ_w is the permittivity of the wall. The region of interest is the domain where the electric field is computed, its size is 310 x 50 µm. h is the height of the PDMS pool. The black rectangles represent the electrodes.

B. Model of the dielectrophoretic force

Close to the electrodes, the electric field is non-uniform. The force induced by a highly non-uniform electric field on a uniform spherical dielectric particle can be derived using Maxwell stress tensor [21] or effective multipole moment [22]. Maxwell stress tensor approach is regarded as the most rigorous one. However, for control purposes, one of the main issue is the computation time. It has been shown in [14] that a good trade-off between the precision of the model and the computation time is given by the dipolar approximation. The dipolar approximation of the i component, $i \in \{x, y\}$, of the dielectrophoretic force induced by an electric field $\mathbf{E}$ can be found in [23, Eq. (8)]:

$$\mathbf{F}_{\text{DEP}} = C_{\text{DEP}} \begin{bmatrix} E_x \frac{\partial E_x}{\partial x} + E_y \frac{\partial E_x}{\partial y} \\ E_x \frac{\partial E_y}{\partial x} + E_y \frac{\partial E_y}{\partial y} \end{bmatrix} \quad (7)$$

where

$$C_{\text{DEP}} = 4\pi\varepsilon_m a^3 K \quad (8)$$

Equation (7) uses the Einstein summation convention: all repeated indexes are summed. The real part of the Clausius-Mossotti factor K is defined as:

$$K = Re\left(\frac{\varepsilon_p^* - \varepsilon_m^*}{\varepsilon_p^* + 2\varepsilon_m^*}\right), \quad (9)$$

where ε_m^* and ε_p^* are the complex permittivity of the medium and the particle, respectively. These are defined as $\varepsilon^* = \varepsilon + j\frac{\sigma}{\omega}$ where ε is the permittivity, σ is the conductivity and $\omega = 2\pi f$ is the angular frequency of the harmonic electric field.

The force calculation requires the determination of the electric field $\mathbf{E}$ in the system. The electric potential ϕ has been formulated in [15, Eq.(6)] . The boundary conditions are specified in Fig. 2 and comes from [15] where details can be found. Thus, the electric potential can be expressed as :

$$\phi(x, y, \mathbf{U}(t)) = \mathbf{e}(x,y)^T \cdot \mathbf{A} \cdot \mathbf{U}, \quad (10)$$

where

$$\begin{cases} \mathbf{e}(x,y)^T = \begin{bmatrix} e_0 & e_1 & ... & e_{P_f} \end{bmatrix} \\ \\ e_0 = \dfrac{h-y}{h} \\ \\ \forall p \in [1, P_f], e_p = \dfrac{e^{p\pi(2h-y)/L} - e^{p\pi y/L}}{e^{2hp\pi/L} - 1} e^{ip\pi x/L} \end{cases} \quad (11)$$

and $\mathbf{U}$ is a N_e vector composed of the electric potentials applied to each electrode, N_e being the number of electrodes. $\mathbf{A}$ is a (P_f, N_e) matrix composed of the $a_{p,n}$ coefficients analytically defined in [15, Table 1] and is only function of the system geometry. P_f is the chosen length of the Fourier series. In this article, the length of the Fourier series is $P_f = 2N_e$ which is, accordingly to [15], a good trade-off between the computation time and the convergence of the Fourier series. $\mathbf{e}(x,y)^T$ is the vector of the P_f exponential terms (Eq 11) evaluated at the position of the object (x,y). L is the width of the electrode pattern. In this formulation, $\mathbf{U}$, the control parameter of the system, and the matrix $\mathbf{A}$, are independent of position (x,y) of the particle. Consequently, the calculation of the gradients of the electric potential, required to determine both the electric field and the dielectrophoretic force, is simple. The electric field is thus:

$$\mathbf{E} = \overrightarrow{\nabla}(\phi) = \begin{bmatrix} \frac{\partial \mathbf{e}^T}{\partial x} \mathbf{A}\mathbf{U} \\ \frac{\partial \mathbf{e}^T}{\partial y} \mathbf{A}\mathbf{U} \end{bmatrix} \quad (12)$$

Based on (7), the dielectrophoretic force can be defined as:

$$\mathbf{F}_{\text{DEP}} = C_{\text{DEP}} \begin{bmatrix} \frac{\partial^2 \mathbf{e}^T}{\partial x^2} \mathbf{A}\mathbf{U} & \frac{\partial^2 \mathbf{e}^T}{\partial x \partial y} \mathbf{A}\mathbf{U} \\ \frac{\partial^2 \mathbf{e}^T}{\partial y \partial x} \mathbf{A}\mathbf{U} & \frac{\partial^2 \mathbf{e}^T}{\partial y^2} \mathbf{A}\mathbf{U} \end{bmatrix} \cdot \begin{bmatrix} \frac{\partial \mathbf{e}^T}{\partial x} \mathbf{A}\mathbf{U} \\ \frac{\partial \mathbf{e}^T}{\partial y} \mathbf{A}\mathbf{U} \end{bmatrix} \quad (13)$$

This expression can also be rewritten as a quadratic function of the control parameter $\mathbf{U}$:

$$\mathbf{F}_{\text{DEP}} = \mathbf{U} \cdot \mathbf{P} \cdot \mathbf{U}^T \quad (14)$$

where:

$$\mathbf{P} = C_{\text{DEP}} \cdot \left(\frac{\partial \mathbf{e}^T}{\partial \mathbf{X}}(x,y) \cdot \mathbf{A}\right)^T \cdot \frac{\partial^2 \mathbf{e}^T}{\partial \mathbf{X}^2}(x,y) \cdot \mathbf{A} \quad (15)$$

and $\mathbf{X} = [x, y]^T$. Eq. (14) makes it possible to calculate the dielectrophoretic force applied to the object whatever its position (x,y) and the control voltages $\mathbf{U}$. The equations (1), (2), (3) and (14) form the direct model of the dielectrophoresis-based micromanipulation platform.

Considering the presented models, the speed of the particle can be expressed as:

$$\dot{\mathbf{X}} = -\mathbf{D}^{-1}(\mathbf{F}_g + \mathbf{U} \cdot \mathbf{P} \cdot \mathbf{U}^T) \quad (16)$$

This analytical model is compared to both simulation and experimental data in the next section. In the rest of this article, the model will be named as FSM for Fourier Series Model
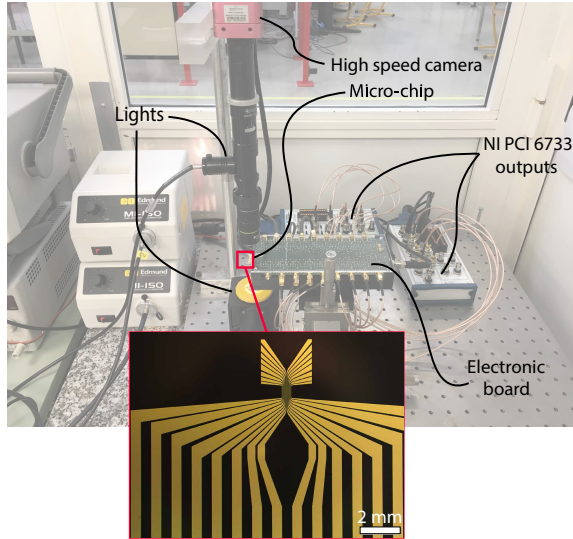
Fig. 3. Picture of the setup used for experiments. The main components are the chip, the high speed camera, the NI PCI analog outputs and the electronic board.
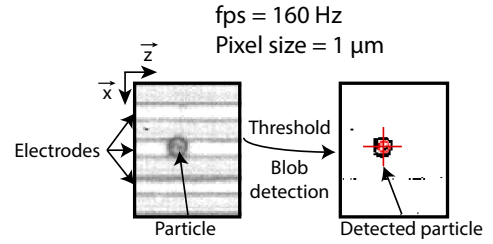

Fig. 4. Picture of a particle above an electrode during an experiment. The particle can be seen thanks to the combination of reflection and transmission enlightenment. The left side represents the image from the camera. The right side of the picture represents the result of the image processing algorithm, composed of a threshold and a blob detection, the center of the cross is the center of the detected particle. The size of a pixel in the image and the fps used for the experiments are specified.

III. DIRECT MODEL VALIDATION

The previous section defines the direct FSM making it possible to compute the motion of the particle when it undergoes a dielectrophoretic force F_{DEP}, induced by given voltages **U**. To evaluate the adequacy of the FSM, it is compared to simulation with the FEM software COMSOL and experiments (section III-B). Data for the FEM simulation, as well as the equipment used for the experiment are given in section III-A.

A. Description of the dielectrophoresis-based platform

As described in Fig. 3, the dielectrophoretic platform is built around a micro-chip fabricated in a clean-room dedicated to microfabrication. This chip is composed of an array of $N_e = 16$ parallel electrodes to enable dielectrophoretic actuation. Each electrode has a width of $10\,\mu$m and the gap between two electrodes is $10\,\mu$m. Electrodes are composed of $20\,$nm of titanium and $200\,$nm of gold deposited using photolithography on a glass wafer. A PDMS (Polydimethylsiloxane) pool, with a thickness around $1\,$mm, is added on top of the chip and sticks by adhesion. This pool is filled with micro-beads of $10\,\mu$m diameter in a solution of PBS (Phosphate-buffered saline) diluted 10 times with a conductivity of $0.2\,$S/m. A droplet of TWEEN20 from SIGMA-ALDRICH is added to minimize adhesion between the chip and the particles. The chip is plugged into a home-made electronic board which independently supplies the electrodes in alternative current. This board multiplies the continuous output of two NI PCI 6733 boards, which are the computed output voltages, with a sinusoidal signal of 1 V_{pp} at a frequency of $50\,$kHz generated by a HAMEG HM8131-2. The NI analog output devices are connected to a computer Dell T3400 with OpenSuse 13.2 operating system, and a kernel 2.6 patched with RTAI3.8.1 to achieve real time performances. This computer is also used to grab images from a high speed camera Photon Focus MV-D 1024 at 160 fps with a pixel resolution of $1\,\mu$m

(Fig. 4) allowing accurate in-line tracking. It is also used to process information and to compute the output voltages. To facilitate the image processing and enable the observation of particles above the electrodes, the chip is enlightened by reflection and transmission, giving the images in Fig. 4. With this enlightenment, a threshold followed by a blob detection algorithm allows us to track particles. The result of the image processing is also given in Fig. 4. The control algorithm is implemented in C++. The threshold and blob detection algorithm are realised without external library. It allows going through each pixel only once to process the image and limit computation time. The number of iterations to compute the direct FSM is quadratically dependent on the number of electrodes.

B. Evaluation of the presented FSM model

This section presents the validation of the direct FSM through comparison with FEM (Finit Element Model) simulations and experiments.

1) Comparison with FEM

As a first validation step, the model is compared to a finite element simulation from COMSOL software using the electrostatic module. The chosen boundary conditions are zero charge accumulation, on the walls and between the electrodes, and charge conservation inside the simulated area. For the simulation, a particle of $10\,\mu$m of diameter, $\epsilon_m = 78$ and $K = -0.5$ were considered. The 6th electrode, between 100 and $110\,\mu$m (see Fig. 5a), is supplied with a sinusoidal signal of 5V at $50\,$kHz. The other electrodes are set to 0V. The Fig. 5a shows the magnitude of the DEP force on $\vec{x}$ computed by the FSM in the $(\vec{x},\vec{y})$ plane. The magnitude of the force is represented through the color range. In the yellow area, $F_{\text{DEP}_{\text{model}},x} \geq 2.10^{-11}$N, inducing a displacement to the right. In the purple area, $F_{\text{DEP}_{\text{model}},x} \leq -2.10^{-11}$N, inducing a displacement to the left.

Fig. 5b uses the same color range to represent the difference in magnitude following $\vec{x}$ between the FSM and FEM. The arrows represent the direction of the DEP force in the $(\vec{x},\vec{y})$ plane for the FSM (black arrows) and the FEM (red arrows). Fig. 5b shows that the computed magnitude of the actuation force is similar close to the supplied electrode. Then, we can observe an error around 40% in the further area. The dotted
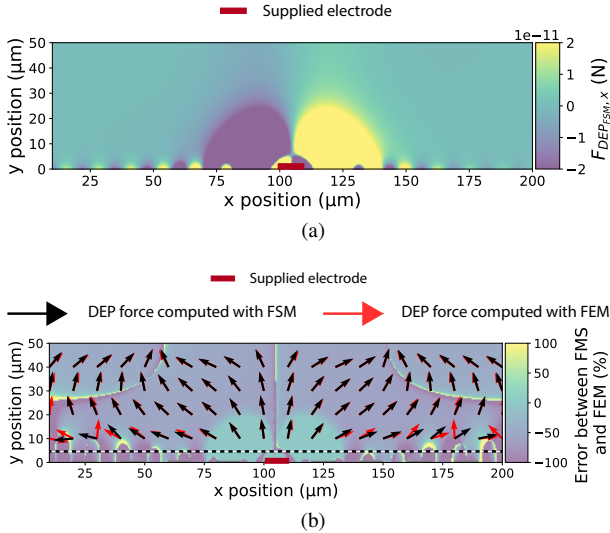
(a)

(b)

Fig. 5. Comparison between the FSM and FEM. The electrode between 100 and 110 μm is supplied with a sinusoidal signal of 5V at 50 kHz while the others are set to 0V. (a) Represents the value of the DEP force following $\vec{x}$ axis. In the yellow area, $F_{\text{DEP}_{\text{model}},x} \geq 2.10^{-11}$N, inducing a displacement to the right. In the purple area, $F_{\text{DEP}_{\text{model}},x} \leq -2.10^{-11}$N, inducing a displacement to the left (b) Represents the error in percentage of the DEP force following $\vec{x}$ between the FSM and FEM. Arrows represent the DEP force direction in the $(\vec{x},\vec{y})$ plane

line represents $y =5\,\mu$m, which is the minimum altitude of the controlled particle. Next to the actuated electrodes, where the DEP force is significant, the force directions established by the two models are in coherence (Fig. 5b). Arrows only show differences after 170 μm. At this location, the absolute magnitude of the DEP force following the $\vec{x}$ axis is inferior to 10^{-14}N and can be neglected. The next subsection will compare the calculated motion of a particle predicted by our model to an experiment.

2) Comparison with experimental data

The second validation of the FSM is a comparison with experimental data. A simulation using the FSM and the following procedure is done: at $t = 1s$, an actuation signal consisting in a step voltage of 3 V at 50 kHz is applied to the electrode closest to the particle (20 to 30 μm in Fig. 6). After 1.5 s the electrode is switched off and the one between 80 and 90 μm is supplied with the actuation signal. This cycle is repeated 3 times. In the model, the chosen initial altitude of the particle $y^{init} = 7\,\mu$m and the anisotropic drag force model is considered. In parallel, an experiment following the same procedure was done using a borosilicate micro-bead of 10 μm of diameter. Results are given in Fig. 6. They show that the calculated position is coherent with the experiment, meanwhile, the FSM has a tendency to slightly overestimate the speed as it can be observed at $t = 4.2\,s$. This can be induced by several factors, such as the uncertainties of the model (related to the properties of the particle, of the medium or the electrodes), or the chosen boundary conditions as discussed in [24].

The mean position error between the simulated and experimental curve on 1 cycle is less than 1 μm with a standard deviation of 4.5 μm, which is half of the diameter of the used particle and seems promising for the control.
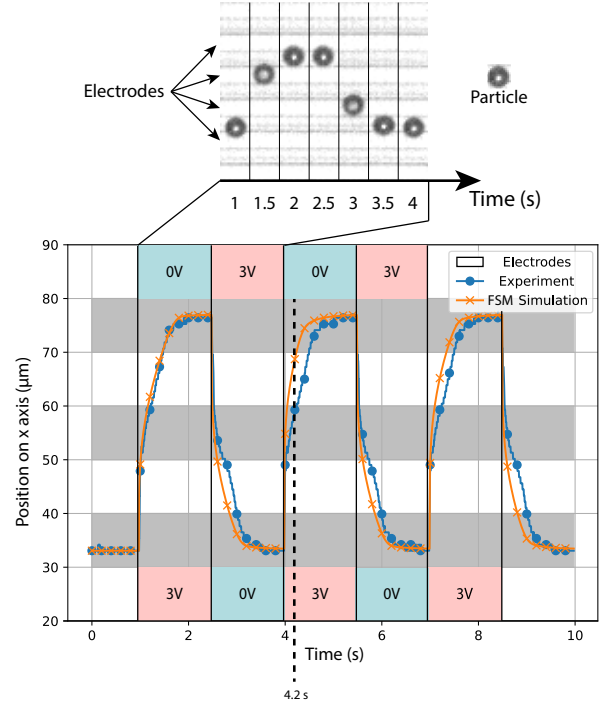

Fig. 6. Experimental validation of the FSM through response to steps of 3 V. At t = 0 s, all electrodes (in white on the graph), are set to 0 V. At t = 1 s, the bottom electrode is set to 3 V, then each 1.5 s, the voltage of the bottom and the top electrode is switched. The dotted curve represents the trajectory followed by the particle during the experiment while the crossed curve is the trajectory obtained through simulation using the proposed model. The top part of the figure is composed of images taken during the experiment.

IV. MODEL INVERSION DEFINITION AND VALIDATION

Following a reference trajectory requires to define at any time t, a control voltage $\mathbf{U}$ enabling to induce the desired velocity $\dot{\mathbf{X}}$ to the particle. In other words, it means to find a solution $\mathbf{U}$ of the quadratic equation (16) knowing $\dot{\mathbf{X}}$. We propose a numerical method to solve this equation in a short time in order to be used in the control loop.

A. Inversion of the FSM model

The keypoint in the inversion of Eq. (16) is the quadratic expression $\mathbf{U} \cdot \mathbf{P} \cdot \mathbf{U}^T$ corresponding to $\mathbf{F}_{\text{DEP}}$ as defined in Eq.(14). In addition, for practical reasons, the voltages applied to each electrode are limited to an upper bound value $\mathbf{U}_{\max}$ inducing a second non-linearity. When particles moved at high speed, or close to the electrodes, both non-linearities (quadratic function and saturation) have to be taken into account and the inversion of the model requires a numeric method [25].

The numerical inversion of the FSM consists in finding a vector of voltages $\mathbf{U}$ which minimizes the cost function:

$$f_{\text{cost}}(\mathbf{U}) = ||\mathbf{F}_{\text{DEP}}^{\text{Des}} - \mathbf{F}_{\text{DEP}}(\mathbf{U})||. \quad (17)$$

As proposed by Michálek *et al.* in a study on a global optimization algorithm [26], the simulated annealing method appears to be the most precise and one of the fastest in the framework of dielectrophoresis. We propose to use this numerical method to invert our FSM model.
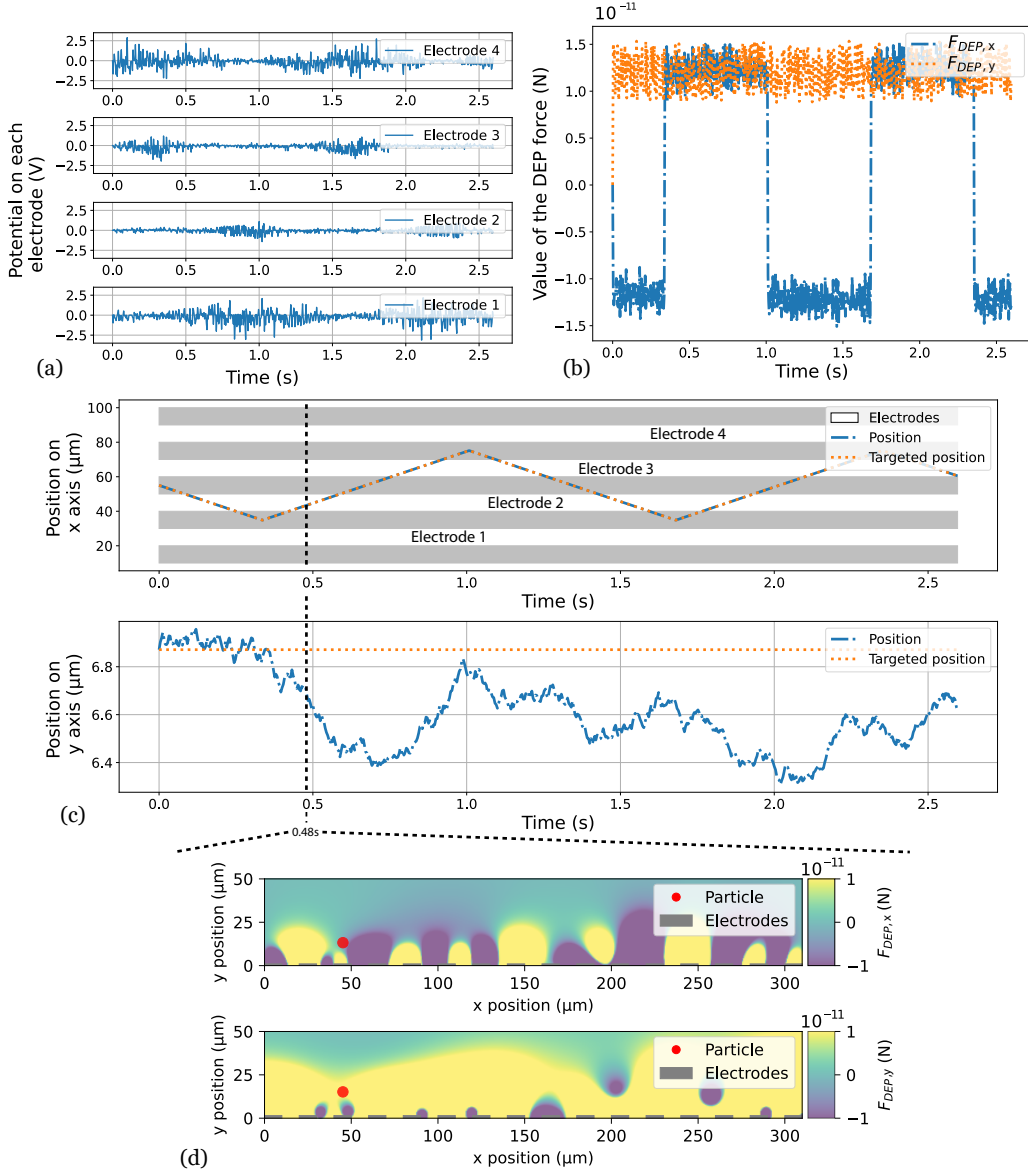
Fig. 7. Validation of the inverse model through a simulation. The targeted trajectory is a saw shape with a slope of $60\,\mu\text{m/s}$ on $\vec{x}$ and a constant altitude on $\vec{y}$. a) Voltage applied to the electrodes closest to the particle. b) Dielectrophoretic force applied to the particle along $\vec{x}$ and $\vec{y}$ axes. Even if the voltage applied to the electrodes varies constantly, the dielectrophoretic force applied to the particle can be constant. Indeed, for a position (x,y) it exists several $\mathbf{U}$ inducing the same force. c) Targeted trajectory and simulated one on $\vec{x}$ and $\vec{y}$. d) Spatial simulation of the DEP force inside the micro-chip at t=0.48s computed by the FSM. The color range represents the magnitude of the DEP force along $\vec{x}$ on the upper image and $\vec{y}$ on the bottom one.

The annealing method is a probabilistic technique to approximate the global minimum of a cost function $f_{\text{cost}}(\mathbf{U}) = E$, where E is called "the energy of the system". A second parameter T, called "temperature", is also considered and decreases with time, starting from an initial value T_{init}. At each time step, some neighboring values $\mathbf{U}^*$ of the current control signal $\mathbf{U}$ are considered and the energy E of each $\mathbf{U}^*$ is compared to the current energy of $\mathbf{U}$. In most of the cases, the algorithm chooses the control signal that decreases the energy E in order to converge to the minimum energy value. However, in order to avoid local minima, some modifications that increase the energy E are randomly accepted depending on the system temperature T. Indeed, as the temperature reduces, the algorithm will decreases the probability to explore control parameters inducing a growing energy.

In our case, the errors along the $\vec{x}$ and $\vec{y}$ axis can be decoupled, the chosen cost function (17) becomes:

$$f_{\text{cost}}(\mathbf{U}) = \alpha_{\text{x}}|F_{\text{x}}^{\text{Des}} - F_{\text{x}}(\mathbf{U})| + \alpha_{\text{y}}|F_{\text{y}}^{\text{Des}} - F_{\text{y}}(\mathbf{U})|, \quad (18)$$

where $F_{\text{x}}^{\text{Des}}$ (resp. $F_{\text{y}}^{\text{Des}}$) is the desired force following $\vec{x}$ axis (resp. $\vec{y}$ axis). $F_{\text{x}}(\mathbf{U})$ (resp. $F_{\text{y}}(\mathbf{U})$ is the calculated force on $\vec{x}$ (resp. $\vec{y}$) generated by the voltages $\mathbf{U}$. α_{x} and α_{y} manage the relative importance between the error along $\vec{x}$ and along $\vec{y}$. We chose to increase the weight of the error along $\vec{x}$ by choosing $\alpha_{\text{x}} = 2/3$ and $\alpha_{\text{y}} = 1/3$.

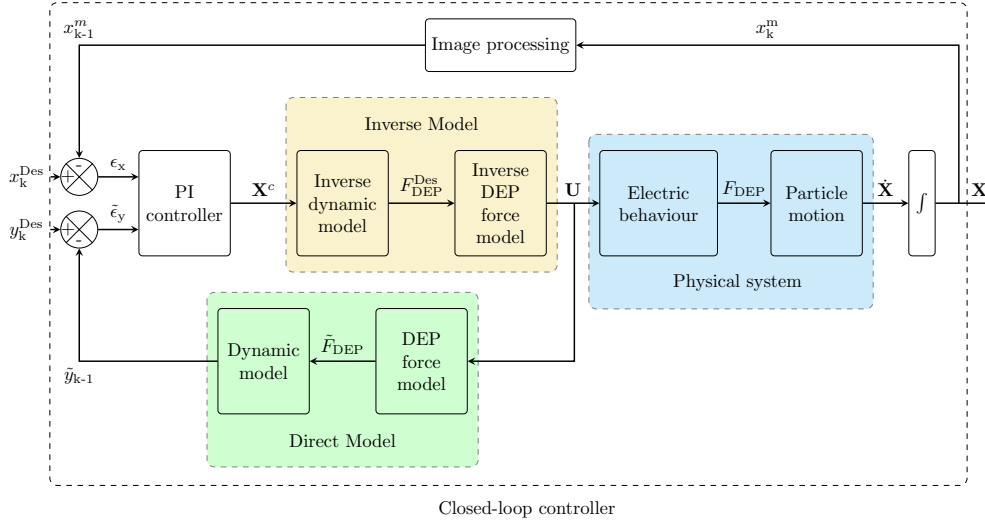T is decreasing following the law:

$$T = T_{\text{init}}e^{-t.10^{-4}} \quad (19)$$

Fig. 8. Block diagram of the closed-loop controller. A desired position $\mathbf{X}^{\text{Des}}$ is the input. The error ϵ_{x} and $\tilde{\epsilon}_{\text{y}}$ are built using the available measure x^m along $\vec{x}$ and using the reconstruction of the experimental position $\tilde{y}$ along $\vec{y}$. A PI controller computes the error ϵ to obtain the $\mathbf{X}^c$, the input vector of the inverse model. The calculated voltages $\mathbf{U}$ are then applied to the physical system inducing the particle motion measured by image processing.

The algorithm stops when the following criteria is reached:

$$E = f_{\text{cost}}(\mathbf{U}) < \epsilon_{\text{stop}}, \qquad (20)$$

where ϵ_{stop} optimal value will be discussed in section V.

The introduced annealing method defined by equations (18), (19), (20), enables to define a numerical model of the voltages $\mathbf{U}$ to apply as a function of a desired $\mathbf{F}_{\text{DEP}}^{\text{Des}}$. This model is called inverse FSM model in the following.

B. Validation of the inverse FSM

We are going to illustrate the behaviour and show the relevance of the inverse FSM model on an example. We consider a chip composed of N_{e} =16 parallel electrodes of $10\,\mu\text{m}$ width, spaced by $10\,\mu\text{m}$. The considered particle is a borosilicate micro-bead of $10\,\mu\text{m}$ in diameter. We are going to simulate a desired saw shape trajectory with a slope of $60\,\mu\text{m/s}$ on $\vec{x}$ and a constant altitude on $\vec{y}$.

A saw shape trajectory enables to characterize the precision of the applied force (on the constant slope parts) and the ability of the proposed system to induce high dynamics on a particle (instantaneous change of direction). The constant target on $\vec{y}$ ensures that the particle stays in the focal plane of the camera to have a better precision during image processing.

The temporal and spatial results of the FSM simulation can be seen in Fig. 7. In order to follow the reference saw shape trajectory, the voltages $\mathbf{U}$ are determined using the inverse FSM (See the voltage values of the four electrodes close to the reference trajectory on Fig. 7a). The voltages induce a DEP force on the particle whose components along $\vec{x}$ and $\vec{y}$ are described on Fig. 7b. It can be noticed that several $\mathbf{U}$ can produce a similar DEP force on the particle for the same particle position (x,y). The simulated DEP force enables to determine the particle velocity using the dynamic model (Eq. 16). Fig. 7c shows that in simulation, the inverse FSM enables the particle to follow the reference trajectory with a maximum error of $0.08\,\mu\text{m}$ on $\vec{x}$ and $0.5\,\mu\text{m}$ on $\vec{y}$. At each time step t, it is also possible to visualize the spatial distribution of $\mathbf{F}_{\text{DEP}}$ defined in (Eq. 14). As an example, both components $\vec{x}$ and $\vec{y}$ of $\mathbf{F}_{\text{DEP}}$ at $t = 0.48s$ are described in Fig. 7d. First, it shows that several equilibrium positions can be reached on $\vec{x}$ (See top part of Fig. 7d) demonstrating that the proposed method would be able to control several particles at the same time. Secondly, it clearly appears that the DEP force along $\vec{y}$ above the electrodes (see the bottom part of Fig. 7d) is mostly positive as usually assumed in negative dielectrophoresis ($K < 0$). However, it can locally have a negative value (e.g at location $(x, y) = (205\mu m, 20\mu m)$), meaning that the particle can be locally attracted by the electrodes substrate. We show that it is possible to locally generate an attractive DEP force in negative dielectrophoresis with a combination of several electrodes having independent voltages.

This inverse FSM model can thus be used to implement a closed-loop control, as presented in the next section.

V. CLOSED-LOOP ACTUATION

In order to precisely control a particle along a reference trajectory, we use a vision-based closed-loop controller (Fig. 8). We consider a desired position $X^{\text{Des}} = \begin{bmatrix} x^{\text{Des}} & y^{\text{Des}} \end{bmatrix}^T$ as the input. The error $\epsilon = \begin{bmatrix} \epsilon_x & \tilde{\epsilon}_y \end{bmatrix}^T$ is built using the available measure x^m along $\vec{x}$ and using the reconstruction of the experimental position $\tilde{y}$ along $\vec{y}$. Indeed, the measure along $\vec{y}$ is not accessible in our device as it requires the use of advanced microscopes or image processing [27]. A PI controller computes the error ϵ to obtain the reference position $\mathbf{X}^c$, enabling to determine $\mathbf{F}_{\text{DEP}}^{\text{Des}}$ via the inverse dynamic model and the required voltages $\mathbf{U}$ via the inverse FSM model. The calculated voltages $\mathbf{U}$ are then applied to the physical system inducing the particle motion measured by image processing (see Fig. 8). The control is mainly in 1D and the reference trajectories to follow are provided along $\vec{x}$. However, as the generated DEP force along $\vec{x}$ and $\vec{y}$ are coupled, the position
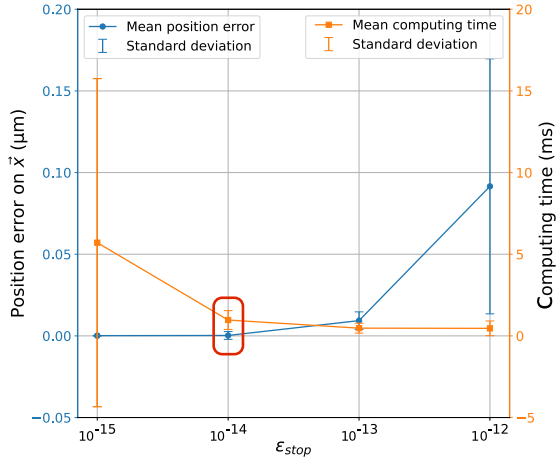
Fig. 9. Determination of the parameters of the simulated annealing algorithm. Computation time required to inverse the model and position error for different values of ϵ_{stop}. Those data are obtained through open-loop simulations where the target is a saw shape trajectory with a slope of $60\,\mu\text{m/s}$ and a range of $40\,\mu\text{m}$ with a constant altitude. The dotted curve represents the mean position error value on $\vec{x}$ and the standard deviation. The squared curve is the mean computing time and the standard deviation. Each point is obtained for a different value ϵ_{stop}. The chosen value is $\epsilon_{\text{stop}} = 1.10^{-14}$.
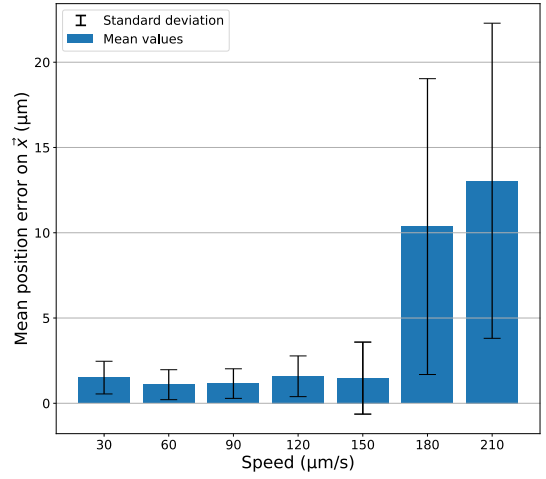

Fig. 10. Results of experiments in closed-loop representing the mean difference and the standard deviation between the particle and the targeted trajectories. The targets are saw shape trajectories with slopes of 30, 60, 90, 120, 150, 180 and $210\,\mu\text{m/s}$.

of the particle on $\vec{y}$ is needed to compute the DEP force on $\vec{x}$. Thus, The trajectory of the particle on $\vec{y}$ is estimated with the FSM model.

A. Definition of the parameters of the FSM model inversion

Two main parameters must be tuned to obtain good results while using the simulated annealing approach. The first one is the control loop sampling frequency f_{cl}, and the second one is the stopping condition ϵ_{stop} (Eq. 20). Indeed, the particularity of the annealing optimization technique is its possibility to deliver sub-optimal solutions if the convergence time is not sufficient. To limit this risk, the algorithm must have enough time to converge. It requires that the control loop sampling time is larger than the time required by the algorithm to converge. Indeed, during a control period, $\frac{1}{f_{\text{cl}}}$, the program must be able to perform the following tasks: to process the image, to minimize the energy of the system and to apply voltages. The largest computational time is the simulated annealing algorithm. On the other hand, the control loop frequency must be high enough to maintain the performances of the closed-loop system. This trade-off will be discussed in the following.

To define the best value of ϵ_{stop} (Eq. 20), open-loop simulations have been performed. The targeted trajectory is a saw shape trajectory of slope $60\,\mu\text{m/s}$ with a range of $40\,\mu\text{m}$ along $\vec{x}$ and a constant position $y^{\text{Des}} = y^{\text{init}}$ along $\vec{y}$. The computation time of the inverse FSM model and the precision on $\vec{x}$ are computed for different values of ϵ_{stop} (See in Fig. 9). The value $\epsilon_{\text{stop}} = 10^{-14}$ seems to be a good compromise. Indeed, with a higher value, the computation time stays under $5\,\text{ms}$ but the precision decreases. A lower value leads to a large uncertainty of the computing time making difficult to determine the control-loop frequency f_{cl}. Considering $\epsilon_{stop} = 10^{-14}$, the mean computation time is around $1.3\,\text{ms}$. Taking into account

the computing time of the image processing and considering that f_{cl} must be at least 2 times lower than the total computing time, the chosen frequency for the closed-loop is $f_{\text{cl}} = 160\,\text{Hz}$ and will be used for the experiments presented in the following section.

B. Experimental results

Using the previously defined closed-loop parameters, experiments are conducted. Saw shape trajectories with a magnitude of $40\,\mu\text{m}$ and slopes of 30, 60, 90, 120 and 150 $\mu\text{m/s}$ on $\vec{x}$ and a constant position $y^{\text{Des}} = y^{\text{init}}$ along $\vec{y}$ are used as reference trajectories. The measured position of the particle x^m on $\vec{x}$ is given by the image processing. The algorithm estimates the position of the particle $\tilde{y}$ based on the FSM model, highlighting the importance of the estimation of the initial altitude. The results in Fig. 6 shows that $y^{init} = 7\,\mu\text{m}$ is coherent and is chosen as the initial altitude. Please note that in order to avoid electrolysis, a $50\,\text{kHz}$ sinusoidal signal is used with a maximum magnitude $U_{\text{max}} = 5V$. For technical reasons, the control is only performed using 8 electrodes. Nevertheless, to demonstrate the performance of the FSM model with numerous electrodes, all the 16 electrodes are considered while computing the voltages. Even if all the voltages are computed, eight electrodes are thus not supplied. Since they are far from the particle and their influence is negligible, and the control remains possible.

The results are presented in Fig. 10 and 11. On Fig. 10 the plotted values are the mean error in position following $\vec{x}$ and the standard deviation between the experimental trajectory and the real time reference trajectory ("target real time" in Fig. 11). Up to $150\,\mu\text{m/s}$ the control allows a precision below $1.5\,\mu\text{m}$ with a maximum standard deviation of $2\,\mu\text{m}$. Above this speed, the algorithm is slower to converge than the control loop frequency f_{cl}. In such extreme cases, the chosen strategy is to let the algorithm converge even if it is longer than $\frac{1}{f_{\text{cl}}}$. Thus, an accumulation of delay between "target computer
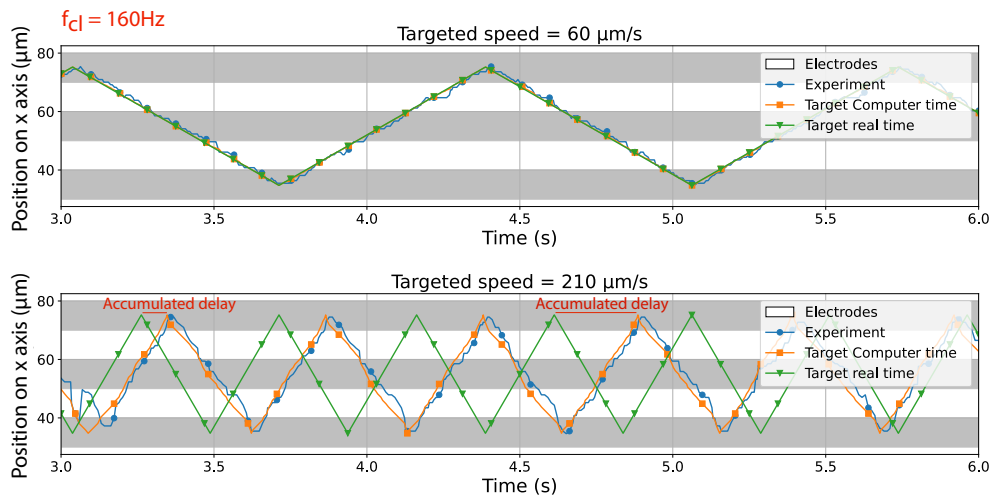
Fig. 11. Comparison of trajectories during an experiment in closed-loop. "Experiment" (The dotted curve) represents the position of the particle through the experiment. "Target computer time" (The squared curve) is the targeted trajectory with the computer time as reference. "Target real time" (The curve with triangle) is the targeted trajectory where each position is precisely spaced by $6.25\,\mathrm{ms}$. In the plot for $60\,\mu\mathrm{m/s}$ the three curve are closed, the obtained precision during this experiment is shown on Fig. 10. For the plot at $210\,\mu\mathrm{m/s}$, the accumulated delay between the two targeted trajectories represents a higher computation time than the control loop frequency, leading to a loss of the real time computing. However, the particle is following the commands sent by the computer (represented by the squared curve) allowing a path tracking without time constraint.

time" and "target real time" occurs for $210\,\mu\mathrm{m/s}$. The "target computer time" (squared curve on Fig. 11) is the reference trajectory concretely sent to the system by the computer. In this case, the simulated annealing algorithm takes too much time to converge and the next control voltage $\mathbf{U}$ is not sent after $1/f_\mathrm{cl} = 6.25ms$. This phenomenon induces an accumulation of delay observable through the increasing gap between the curve "target computer time" and "target real time" (curve with triangle). However, the observed trajectory is still close to the reference based on the computer time with a mean precision below $1\,\mu\mathrm{m}$ and a standard deviation of $2.1\,\mu\mathrm{m}$. It means that the calculated control voltage for a $210\,\mu\mathrm{m/s}$ trajectory is relevant but the computation time is too long to be implemented in a closed loop control.

As a conclusion, until a speed of $150\,\mu\mathrm{m/s}$, trajectory control of particles of $10\,\mu\mathrm{m}$ with an error below $1.5\,\mu\mathrm{m}$ can be reached with the proposed method.

VI. CONCLUSIONS & PERSPECTIVES

This article proposes a closed loop-control strategy of dielectrophoresis-based micromanipulation platforms composed of numerous parallel electrodes. The controller is based on an inverse model using annealing optimization technique. We show that the calculation time, in most cases, is shorter than $5\,\mathrm{ms}$. Based on this inverse model, controlled trajectories are experimentally performed with a control loop frequency of $160\,\mathrm{Hz}$. It is shown that it is possible to control the trajectory of a $10\,\mu\mathrm{m}$ microbead along a reference trajectory up to $150\,\mu\mathrm{m/s}$ with a mean error of $1.5\,\mu\mathrm{m}$, approximately equal to a tenth of the particle diameter, and a maximum standard deviation of $2\,\mu\mathrm{m}$. Close to the electrodes, highly non-linear electric fields are produced, which has the advantage of potential high velocity displacements. However, the altitude of the objects is more complex to predict as vertical displacements are also faster. As the current performance is directly

linked to the computation time of the annealing optimisation method, future work will focus on the improvement of the computation capability of our experimental setup to increase its performance and enable it to converge faster with a better precision. Hardware modifications (increase of RAM or use of newer CPU) as well as other computational methods (parallel computing) are considered. Further developments will also include the extension of this system for the control in the two directions of the electrode plane. The future chip will be composed of two layers of electrodes. With those improvements, our future work will then concentrate on the control of biological cells using this platform, in the framework of the development of controlled lab-on-chip devices.

REFERENCES

[1] X. Dong and M. Sitti, "Controlling two-dimensional collective formation and cooperative behavior of magnetic microrobot swarms," *The International Journal of Robotics Research*, vol. 39, no. 5, pp. 617–638, Apr. 2020. [Online]. Available: http://journals.sagepub.com/doi/10.1177/0278364920903107

[2] A. Demircali, R. Varol, G. Aydemir, E. N. Saruhan, K. Erkan, and H. Uvet, "Longitudinal motion modeling and experimental verification of a microrobot subject to liquid laminar flow," *IEEE/ASME Transactions on Mechatronics*, 2021.

[3] D. Zhang, A. Barbot, B. Lo, and G. Yang, "Distributed Force Control for Microrobot Manipulation via Planar Multi-Spot Optical Tweezer," *Advanced Optical Materials*, vol. 8, no. 21, p. 2000543, Nov. 2020. [Online]. Available: https://onlinelibrary.wiley.com/doi/10.1002/adom.202000543

[4] M. Baudoin, J.-L. Thomas, R. A. Sahely, J.-C. Gerbedoen, Z. Gong, A. Sivery, O. B. Matar, N. Smagin, P. Favreau, and A. Vlandas, "Spatially selective manipulation of cells with single-beam acoustical tweezers," *Nature Communications*, vol. 11, no. 1, p. 4244, Dec. 2020. [Online]. Available: http://www.nature.com/articles/s41467-020-18000-y

[5] G. R. Pesch and F. Du, "A review of dielectrophoretic separation and classification of non-biological particles," *ELECTROPHORESIS*, vol. 42, no. 1-2, pp. 134–152, Jan. 2021. [Online]. Available: https://onlinelibrary.wiley.com/doi/10.1002/elps.202000137

[6] W. Liu, Y. Ren, Y. Tao, Z. Zhou, Q. Wu, R. Xue, and B. Yao, "Multiple frequency electrothermal induced flow: theory and microfluidic applications," vol. 53, no. 17, p. 175304, feb 2020. [Online]. Available: https://doi.org/10.1088/1361-6463/ab71b1

[7] E. A. Henslee, "Review: Dielectrophoresis in cell characterization," *ELECTROPHORESIS*, vol. 41, no. 21-22, pp. 1915–1930, 2020.

[8] W. Waheed, A. Alazzam, A. N. Al-Khateeb, and E. Abu-Nada, "Multiple Particle Manipulation under Dielectrophoresis Effect: Modeling and Experiments," *Langmuir*, vol. 36, no. 12, pp. 3016–3028, Mar. 2020. [Online]. Available: https://pubs.acs.org/doi/abs/10.1021/acs.langmuir.0c00187

[9] M. Kharboutly and M. Gauthier, "High speed closed loop control of a dielectrophoresis-based system," in *2013 IEEE International Conference on Robotics and Automation*. Karlsruhe, Germany: IEEE, May 2013, pp. 1446–1451. [Online]. Available: http://ieeexplore.ieee.org/document/6630761/

[10] J. Zemánek, T. Michálek, and Z. Hurák, "Phase-shift feedback control for dielectrophoretic micromanipulation," *Lab on a Chip*, vol. 18, no. 12, pp. 1793–1801, 2018. [Online]. Available: http://xlink.rsc.org/?DOI=C8LC00113H

[11] T. Michálek, A. Bolopion, Z. Hurák, and M. Gauthier, "Control-oriented model of dielectrophoresis and electrorotation for arbitrarily shaped objects," *Physical Review E*, vol. 99, no. 5, p. 053307, May 2019. [Online]. Available: https://link.aps.org/doi/10.1103/PhysRevE.99.053307

[12] T. Michálek and Z. Hurák, "Position and orientation control at micro- and mesoscales using dielectrophoresis," *arXiv:2002.08764 [cs, eess]*, Feb. 2020, arXiv: 2002.08764. [Online]. Available: http://arxiv.org/abs/2002.08764

[13] P. Keller, "Unravelling tumour heterogeneity by single-cell profiling of circulating tumour cells," *Nature Reviews Cancer*, 2019.

[14] V. Gauthier, A. Bolopion, and M. Gauthier, "Comparison of Dynamic Models for Non-Contact Micromanipulation Based on Dielectrophoretic Actuation," in *2018 IEEE/RSJ International Conference on Intelligent Robots and Systems (IROS)*. Madrid: IEEE, Oct. 2018, pp. 4869–4874. [Online]. Available: https://ieeexplore.ieee.org/document/8594377/

[15] Vladimir Gauthier, Aude Bolopion, and Michaël Gauthier, "Analytical Formulation of the Electric Field Induced by Electrode Arrays: Towards Automated Dielectrophoretic Cell Sorting," *Micromachines*, vol. 8, no. 8, p. 253, Aug. 2017. [Online]. Available: http://www.mdpi.com/2072-666X/8/8/253

[16] A. Zouaghi, N. Zouzou, and L. Dascalescu, "Effect of travelling wave electric field on fine particles motion on an electrodynamic board," in *2017 IEEE Industry Applications Society Annual Meeting*. Cincinnati, OH: IEEE, Oct. 2017, pp. 1–6. [Online]. Available: http://ieeexplore.ieee.org/document/8101701/

[17] J. Zemánek, T. Michálek, and Z. Hurák, "Feedback control for noise-aided parallel micromanipulation of several particles using dielectrophoresis: General," *ELECTROPHORESIS*, vol. 36, no. 13, pp. 1451–1458, Jul. 2015. [Online]. Available: http://doi.wiley.com/10.1002/elps.201400521

[18] M. Kharboutly, M. Gauthier, and N. Chaillet, "Modeling the trajectory of a microparticle in a dielectrophoresis device," *Journal of Applied Physics*, vol. 106, no. 11, p. 114312, Dec. 2009. [Online]. Available: http://aip.scitation.org/doi/10.1063/1.3257167

[19] A. Ambari, B. Gauthier Manuel, and E. Guyon, "Effect of a plane wall on a sphere moving parallel to it," *Journal de Physique Lettres*, vol. 44, no. 4, pp. 143–146, 1983. [Online]. Available: http://www.edpsciences.org/10.1051/jphyslet:01983004404014300

[20] A. Ambari, B. Gauthier-Manuel, and E. Guyon, "Wall effects on a sphere translating at constant velocity," *Journal of Fluid Mechanics*, vol. 149, no. -1, p. 235, Dec. 1984.

[21] X. Wang, X.-B. Wang, and P. R. Gascoyne, "General expressions for dielectrophoretic force and electrorotational torque derived using the Maxwell stress tensor method," *Journal of Electrostatics*, vol. 39, no. 4, pp. 277–295, Aug. 1997. [Online]. Available: https://linkinghub.elsevier.com/retrieve/pii/S0304388697001265

[22] M. Washizu and T. Jones, "Multipolar dielectrophoretic force calculation," *Journal of Electrostatics*, vol. 33, no. 2, pp. 187–198, Sep. 1994. [Online]. Available: https://linkinghub.elsevier.com/retrieve/pii/0304388694900531

[23] T. Jones, "Basic theory of dielectrophoresis and electrorotation," *IEEE Engineering in Medicine and Biology Magazine*, vol. 22, no. 6, pp. 33–42, Nov. 2003. [Online]. Available: http://ieeexplore.ieee.org/document/1304999/

[24] N. Green, A. Ramos, and H. Morgan, "Numerical solution of the dielectrophoretic and travelling wave forces for interdigitated electrode arrays using the finite element method," *Journal of Electrostatics*, vol. 56, no. 2, pp. 235–254, 2002. [Online]. Available: https://www.sciencedirect.com/science/article/pii/S0304388602000694

[25] A. Castellanos, A. Ramos, A. González, N. G. Green, and H. Morgan, "Electrohydrodynamics and dielectrophoresis in microsystems: scaling laws," *Journal of Physics D: Applied Physics*, vol. 36, no. 20, pp. 2584–2597, Oct. 2003. [Online]. Available: https://iopscience.iop.org/article/10.1088/0022-3727/36/20/023

[26] T. Michálek, "Real-time optimization-based control for dielectrophoresis," Czech Technical University in Prague, Tech. Rep., May 2015.

[27] M. Gurtner and J. Zemánek, "Twin-beam real-time position estimation of micro-objects in 3d," *Measurement Science and Technology*, vol. 27, no. 12, p. 127003, nov 2016. [Online]. Available: https://doi.org/10.1088/0957-0233/27/12/127003

Alexis Lefevre received the engineer degree in mechatronics, in 2017, from the national engineering school of Limoges, France. He was an R&D engineer in control system, and then, field engineer on automatic inspection and quality control system. He is currently research engineer at the FEMTO-ST institute. His scientific field is the non-contact actuation of micro-robots using dielectrophoresis.

Vladimir Gauthier received the engineering degree in mechatronics, in 2015, from the national engineering school Supmeca, Paris, France. He then received the Ph.D. degree in robotics from Université de Bourgogne Franche Comté, Besancon, France, in 2018. He was a member of the FEMTO-ST Institute, where he developed control laws for the manipulation of micrometer size objects by dielectrophoretic effects.

Michaël Gauthier CNRS senior scientist, works in the field of micro-nanorobotics since 2000 and has proposed, modeled and experimented new robotics tools for microhandling and micro-assembly in several European and National projects. He is the president of the French-Swiss Alliance between FEMTO-ST and EPFL named SMYLE. During the last years, he was the head of the micro-nanorobotics department in FEMTO-ST (2012-16) and vice-director of FEMTO-ST institute (2016-19). He is the author of 2 books, more than 40 papers and 60 conference talks. He is also the co-founder of the spin-off 'Percipio Robotics' providing micro-assembly platforms for industrial applications.

Aude Bolopion received her Ph.D. degree in robotics in 2010 from Sorbonne University (ex.Pierre et Marie Curie University), Paris, France. She was a member of the ISIR Institute. Her research interests were focused on teleoperation and haptic feedback at the nanoscale. She got a CNRS researcher permanent position at the FEMTO-ST Institute, Besancon, France in 2011. She received the CNRS bronze medal in 2019 for her work on non contact actuation for microrobotics.